Heliyon 10 (2024) e32458

Contents lists available at ScienceDirect

Heliyon

journal homepage: www.cell.com/heliyon

Research article

Piezo1 – Serine/threonine-protein phosphatase 2A – Cofilin1 biochemical mechanotransduction axis controls F-actin dynamics and cell migration

Francesco Morena [a], Chiara Argentati [a], Silvia Caponi [b], Ines Lüchtefeld [c], Carla Emiliani [a], Massimo Vassalli [d], Sabata Martino [a,*]

[a] Department of Chemistry, Biology, and Biotechnologies, Via del Giochetto, University of Perugia, Perugia, Italy
[b] CNR, Istituto Officina dei Materiali-IOM c/o Dipartimento di Fisica e Geologia, University of Perugia, Perugia, Italy
[c] Laboratory for Biosensors and Bioelectronics, ETH Zürich, Switzerland
[d] James Watt School of Engineering, University of Glasgow, UK

A B S T R A C T

This study sheds light on a ground-breaking biochemical mechanotransduction pathway and reveals how Piezo1 channels orchestrate cell migration. We observed an increased cell migration rate in HEK293T (HEK) cells treated with Yoda1, a Piezo1 agonist, or in HEK cells overexpressing Piezo1 (HEK + P). Conversely, a significant reduction in cell motility was observed in HEK cells treated with GsMTx4 (a channel inhibitor) or upon silencing Piezo1 (HEK-P). Our findings establish a direct correlation between alterations in cell motility, Piezo1 expression, abnormal F-actin microfilament dynamics, and the regulation of Cofilin1, a protein involved in severing F-actin microfilaments.

Here, the conversion of inactive pCofilin1 to active Cofilin1, mediated by the serine/threonine-protein phosphatase 2A catalytic subunit C (PP2AC), resulted in increased severing of F-actin microfilaments and enhanced cell migration in HEK + P cells compared to HEK controls. However, this effect was negligible in HEK-P and HEK cells transfected with hsa-miR-133b, which post-transcriptionally inhibited PP2AC mRNA expression. In summary, our study suggests that Piezo1 regulates cell migration through a biochemical mechanotransduction pathway involving PP2AC-mediated Cofilin1 dephosphorylation, leading to changes in F-actin microfilament dynamics.

1. Introduction

Piezo1 functions as a transmembrane nonselective cation channel permeable to Ca^{2+} and is dedicated to sensing and transducing mechanical stimuli into biochemical signals within cells [1]. Its mechanosensing activity is influenced by various factors, including ion concentration, fatty acids, lipids, cytoskeleton, and associated proteins such as integrins or other proteins in the plasma membrane [2] or cytosol [3]. Playing a pivotal role in mechanosensing and mechanotransduction [4–7], Piezo1 significantly contributes to the orchestration of cell functions in both physiological [2,7–12] and pathological [2,13,14] contexts.

In recent studies, Piezo1 has emerged as a key player in cell migration, with evidence indicating its involvement in the promotion and inhibition of cell motility. This indicates the channel's ability to respond to and transduce disparate cues depending on the type of tissue/cell, spanning both physiological and pathological conditions. For instance, the overexpression/downregulation of Piezo1 in breast cancer [15], gliomas [16], esophageal squamous cell carcinoma [17], and gastric cancer [18] has been correlated with tumor expansion and regression of tumor invasion. Conversely, the downregulation of Piezo1 in the brains of patients with Multiple Sclerosis was associated with the migration of oligodendrocytes [19], and the loss of Piezo1 accelerated cell migration [20] and the progression

* Corresponding author.
E-mail address: sabata.martino@unipg.it (S. Martino).

https://doi.org/10.1016/j.heliyon.2024.e32458
Received 31 October 2023; Received in revised form 24 May 2024; Accepted 4 June 2024
Available online 5 June 2024

of non-small cell lung cancer. A similar effect was observed in various cell types. The activation of the channel inhibits the migration of 3T3B-SV40 fibroblasts [21] and keratinocytes [22], whereas the deficit of Piezo1 in human T cells [23] interferes with integrin-dependent cellular motility. Additionally, the activation of Piezo1 promotes leukocyte diapedesis [24] and mesenchymal stem cell migration [25]. In this regard, we reported an increase in the migration rate of HEK293T (HEK) cells overexpressing Piezo1 and a drastic decrease in the migration process of Piezo1 knockout HEK cells [26].

Therefore, unraveling the biochemical mechanotransduction mechanisms through which Piezo1 regulates cell migration is crucial for understanding the role of Piezo1 in cell homeostasis and developing new drugs to modulate channel activity in diseased cells. Simultaneously, this endeavor offers potential benefits for gaining insights into the multifaceted molecular events of the migration process, a critical cell biological process that occurs throughout life, such as embryonic development, immune response, and wound healing. In some cases, this process is crucial for the onset and progression of diseases, including cancer.

Cell migration is a well-known phenomenon influenced by chemical and/or physical cues, and is categorized into four modalities: chemotaxis, haptotaxis, topotaxis, and electrotaxis [27,28]. A key step in this process involves the dynamic interplay of cytoskeletal components, which allows cells to extend their leading edges, establish contact with the cell body, retract the cell rear, and ultimately facilitate cell movement [29,30]. In this context, routine polymerization of G-actin into F-actin filaments along with the extrusion of pseudopodia (depolymerization of F-actin to G-actin) has been associated with cell motility [31]. This intricate process may be mediated by certain F-actin-linking proteins such as Cofilin1 [32–34], Gelsolin, and Profilin [35]. Cofilin1 is the primary regulatory protein for F-actin dynamics, orchestrating the polymerization/depolymerization processes [36]. In its unphosphorylated state (active form), Cofilin1 promotes the depolymerization of F-actin into G-actin. Phosphorylation by LIM domain kinase 1 (LIMK1) deactivates Cofilin1 [33,37–42], inhibiting its depolymerization of F-actin. The severing mechanism is rapid, occurring at both the barbed and pointed ends, resulting in filament fragmentation and facilitating nucleation as required [39]. Dephosphorylation of Cofilin1 can is catalyzed by phosphatases such as slingshot (SSH1, SSH2, and SSH3) [40], chronophin (CIN) [41], and serine/threonine-protein phosphatase 2A (PP2A) [42]. Notably, PP2A was found to be downstream of Piezo1 in the MDA-MB-231 breast cancer cell line [43].

Although the interplay between Piezo1 and F-actin has been explored [44], even in the context of cell migration, to our knowledge, there has been no reported direct correlation between Piezo1 and the aforementioned F-actin-linked proteins.

In this study, based on the availability of HEK cells overexpressing Piezo1 and HEK cells with Piezo1 knockout [26], we investigated the biochemical mechanotransduction pathway activated by Piezo1 to control migration. In particular, we evaluated the impact of Piezo1 on F-actin dynamics, with specific exploration of the role of Cofilin1, including the involvement of enzymes that activate (PP2A) and inhibit (LIMK1 [45,46]) the severing function of Cofilin1. Our study demonstrates that Piezo1 directly governs cell migration in HEK cells through a biochemical pathway that regulates F-actin microfilament dynamics mediated by PP2A-dependent modulation of Cofilin1 function.

This research significantly contributes to the understanding of the role of Piezo1 in cellular migration and may pave the way for the development of novel drugs that modulate Piezo1 function in diseases associated with abnormal cellular migration.

2. Results

2.1. Expression and activation of the Piezo1 channel enhance cell migration rates

We performed the study in HEK293T cells that overexpress Piezo1 (HEK + P), HEK293T cells knockout for Piezo1 (HEK-P), and

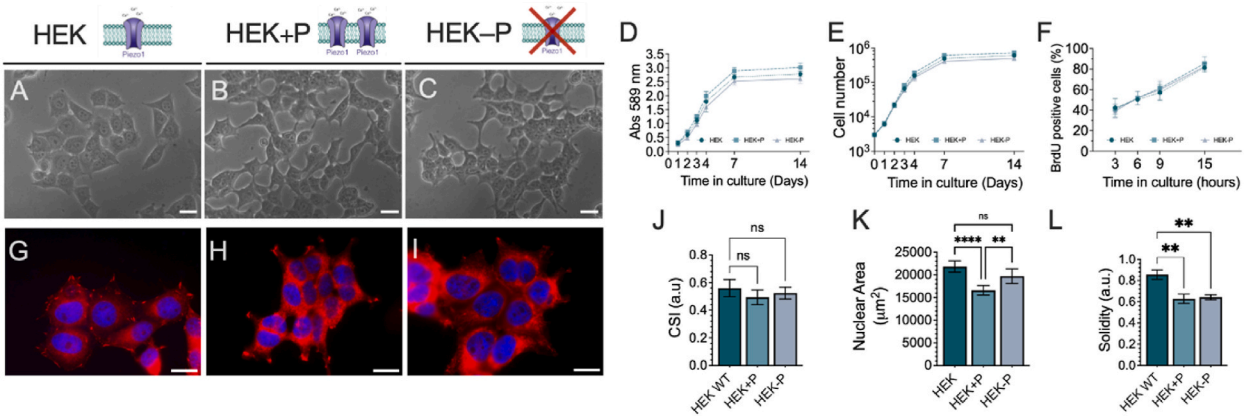

Fig. 1. HEK293T (HEK) cells, HEK overexpressing Piezo1 (HEK + P), and knockout for Piezo1 (HEK-P). A,B,C) Representative phase-contrast microscopy images of HEK, HEK + P, HEK-P. Scale bar 100 μm. D) Cell viability assay, (E) proliferation assay, and (F) BrdU assay in HEK, HEK + P, and HEK-P cells. J,K,L) Computational cytomorphometric measurements of Cell Shape Index (J), Nuclear Area (K), and Solidity (a.u., arbitrary units) (L) in HEK, HEK + P, and HEK-P cells. G,H,I) Immunofluorescence of Vinculin (RED) and nuclei (BLUE) in HEK, HEK + P, and HEK-P cells. Scale bar 20 μm. Results are expressed as mean ± SD of three independent experiments. **P ≤ 0.01; ****P ≤ 0.0001; ns: not significant. (For interpretation of the references to colour in this figure legend, the reader is referred to the Web version of this article.)

HEK293T control cells (HEK) ([26,47,48]; Fig. 1A–C; Fig. S1). The overexpression or knockout of Piezo1 (Fig. S1) did not impact cell viability as evidenced by a comparable mitochondrial dehydrogenase activity curve (Fig. 1D) and growth rate (Fig. 1E). The proliferation doubling-time remained consistent at 16 h for HEK, HEK + P, and HEK-P cells, with BrdU (5′-bromo-2′-deoxyuridine) curves comparable (Fig. 1F). No differences were observed in the Cell Shape Index (CSI) among the three cell types (Fig. 1J), indicating similar overall circular shapes. Reduced Nuclear Area was observed exclusively in HEK + P cells compared to the control cells, as well as compared to HEK-P (Fig. 1K), while decreased Solidity was measured in both HEK + P and HEK-P cells compared to the HEK control (Fig. 1L). This finding is supported by Vinculin staining, which revealed distinct protrusions compared to the HEK control (Fig. 1G–I).

Our previous study demonstrated that disparities in cell migration rates among HEK, HEK + P, and HEK-P became evident after 12 h of culture [26] and persisted consistently over 72 h (Figs. S2A–S2D). In this study, we initiated a more thorough investigation into the migration process, using higher temporal resolution and the drugs that impact the functionality of Piezo1.

We conducted a time course analysis spanning the initial 36 h of the cell migration process in the presence of GsMTx4 [49], a mechanotoxin blocking mechanosensitive ion channels, including Piezo1, and Yoda1 [50], a Piezo1 activator (Fig. 2A–C; Fig. S3). We measured the highest migration rate, 13 μm/h, in the HEK + P cells with a timecourse closing area of ~10 %, ~70 %, and ~90 % at 4 h, 24 h, and 36 h, respectively, as compared to the scratched area at t = 0 h (Fig. 2A–C; HEK + P). HEK cells exhibited a migration rate of 6 μm/h and a closed area of ~5 %, ~30 %, and ~45 % at the same time points (Fig. 2A–C; HEK), while HEK-P cells showed a migration rate of 4 μm/h, and a closed scratch area of ~2 % at 4 h, ~22 % at 24 h, and ~27 % at 36 h (Fig. 2A–C; HEK-P). The treatment of HEK cells with GsMTx4 (2 μM) [26,49] significantly decreased cell migration (closing area ~2 % at 4 h, ~14 % at 24 h, and ~17 % at 36 h; migration rate 4 μm/h) in comparison to the untreated control cells (Fig. 2A–C; HEK + GsMTx4). This treatment mirrored the behavior observed in HEK-P cells (Fig. 2A and B). Conversely, treating HEK cells with Yoda1 (2 μM) [50] significantly enhanced cell migration rate (closing area ~15 % at 4 h, ~50 % at 24 h, and ~60 % at 36 h; migration rate 10 μm/h) compared to the untreated cells (Fig. 2A–C; HEK + Yoda1), mirroring the behavior observed in HEK + P cells (Fig. 2A and B).

The collective data underscored a direct correlation between cell migration and the expression and functionality of Piezo1.

2.2. *Expression and activation of the Piezo1 channel influence cell migration through mechanotransduction, involving F-actin remodeling*

To unveil the molecular mechanotransduction events through which Piezo1 regulates cell migration, we first examined the architecture and length of cytoskeleton F-Actin microfilaments in HEK, HEK + P, and HEK-P cells, both under native state and in the presence of Yoda1.

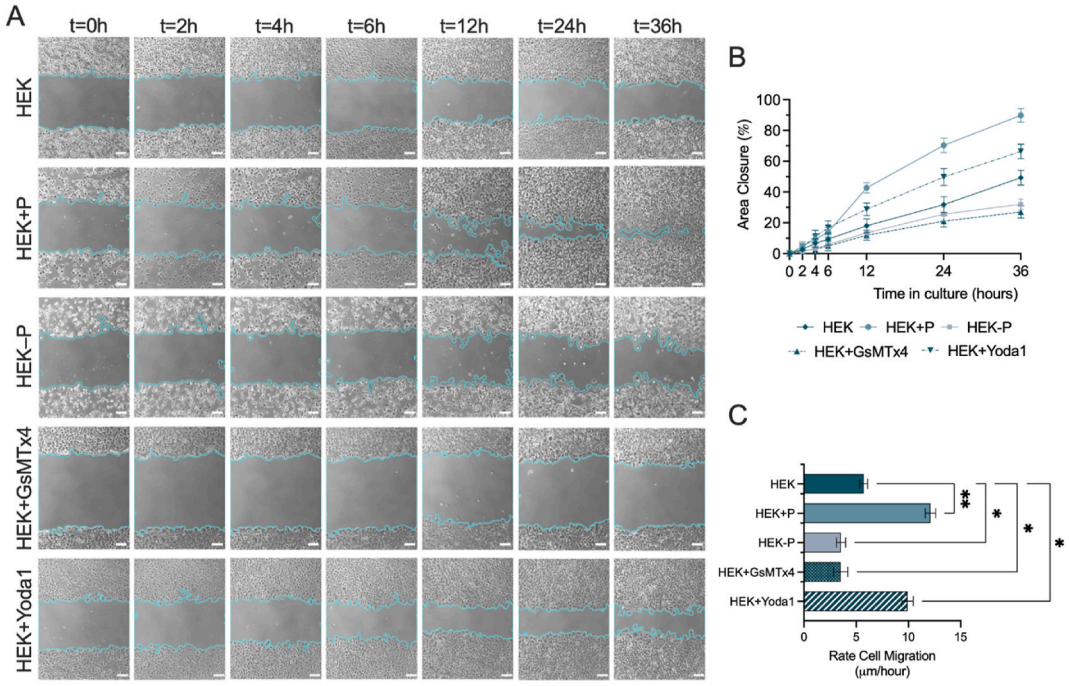

Fig. 2. Time course analysis of cell migration assay in HEK, HEK + P, HEK-P, HEK + Yoda1, and HEK + GsMTx4 cells. A) Representative phase-contrast microscopy images of cell migration in the scratch assay. The scratch area is delimited by cyan lines. Scale bar 100 μm. The closure area of each scratch (B) and the cell migration rate (C) at each time point were measured using the wound healing size tool [51], an image J plugin for the high throughput image analysis of in vitro scratch (Fiji Life Line version 2.0.0, 2018; imagej.net [52]). Results are expressed as mean ± SD of three independent experiments. *P ≤ 0.05; **P ≤ 0.01. (For interpretation of the references to colour in this figure legend, the reader is referred to the Web version of this article.)

The length of F-Actin stress-fibers within the cells is governed by the polymerization and depolymerization process [28,53] offering insights into the variations in F-Actin severing dynamics. In control HEK cells, F-Actin microfilaments displayed canonical organization, with stress-fibers predominantly oriented along the longitudinal cell axis, traversing the cells, and with a mode of 10 μm (Fig. 3A and B; HEK). In contrast, HEK + P cells exhibited extremely short F-Actin stress fibers, with a mode length of 2 μm, and an undefined branching orientation (Fig. 3A and B; HEK + P). Meanwhile, HEK-P cells displayed F-Actin stress-fibers with intermediate characteristics and fragment length with a mode of 6 μm (Fig. 3A and B; HEK-P).

Treatment of HEK cells with Yoda1 resulted in significant remodeling of F-Actin, with stress-fibers fragments exhibiting different lengths (bimodal distribution: 4 μm and 10 μm) and numerous cell protrusions resembling those of HEK + P (Fig. 3C and D). These effects were confirmed in Yoda1-treated HEK + P cells, although no difference in stress-fibers fragmentation length was observed when compared to untreated HEK + P (Fig. 3C and D), suggesting a negligible effect of the treatment of Yoda1 in HEK + P cells. Moreover, no differences in F-Actin stress-fibers fragmentation length were observed in Yoda1-treated HEK-P cells compared to untreated cells (Fig. 3C and D).

To deepen our understanding of the relationship between Piezo1 activation and cytoskeletal reorganization, we conducted a dynamic analysis of actin remodeling following the introduction of the channel's specific agonist, Yoda1. The change in the actin turnover rate was evaluated by measuring the fluorescence intensity of the F-Actin bound fluorescent probe SiR-actin over time [55]: here, a decrease in fluorescent intensity corresponds to an increase in F-Actin turnover rate. The addition of a control solution prompted a modest increase in the F-Actin turnover rate across all cell types (Fig. 4A). In contrast, a more substantial increase is observed immediately in HEK and HEK + P cells after the addition of Yoda1, but not in HEK-P cells. Intriguingly, HEK cells show changes only for a Yoda1 concentration of 1 μM, whereas HEK + P cells respond even to 0.1 μM Yoda1, indicating heightened sensitivity due to Piezo1 overexpression (Fig. 4B).

To assess how these modified F-Actin turnover rates might impact cell stiffness, force spectroscopy curves were obtained by atomic force microscopy-based nanoindentation [56] before and 5 min after the addition of 1 μM Yoda1 (Fig. 4C). In HEK cells, no significant change in stiffness was observed, whereas in treated HEK + P cells, stiffness decreased to a level resembling that of HEK cells. The

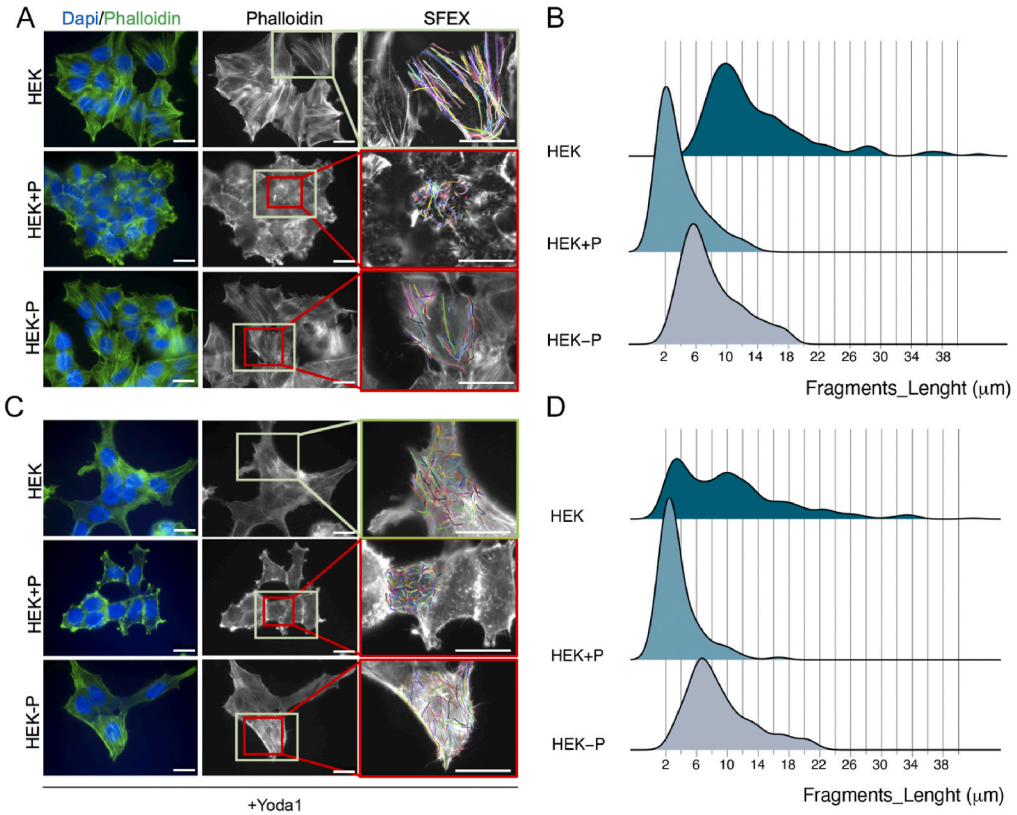

Fig. 3. The architectures of actin fiber microfilaments in HEK, HEK + P, and HEK-P in the absence and presence of Yoda1. A,C) F-Actin microfilaments staining with phalloidin (GREEN) and nuclei with DAPI (BLUE). Scale bar 20 μm. A, C) F-Actin networks were segmented from fluorescence images by using the open-source MATLAB package Stress Fiber Extractor [SFEX] [54]. B,D) Distribution of stress fiber fragment lengths measured with the above-mentioned SFEX. For details see the methods section. (For interpretation of the references to colour in this figure legend, the reader is referred to the Web version of this article.)

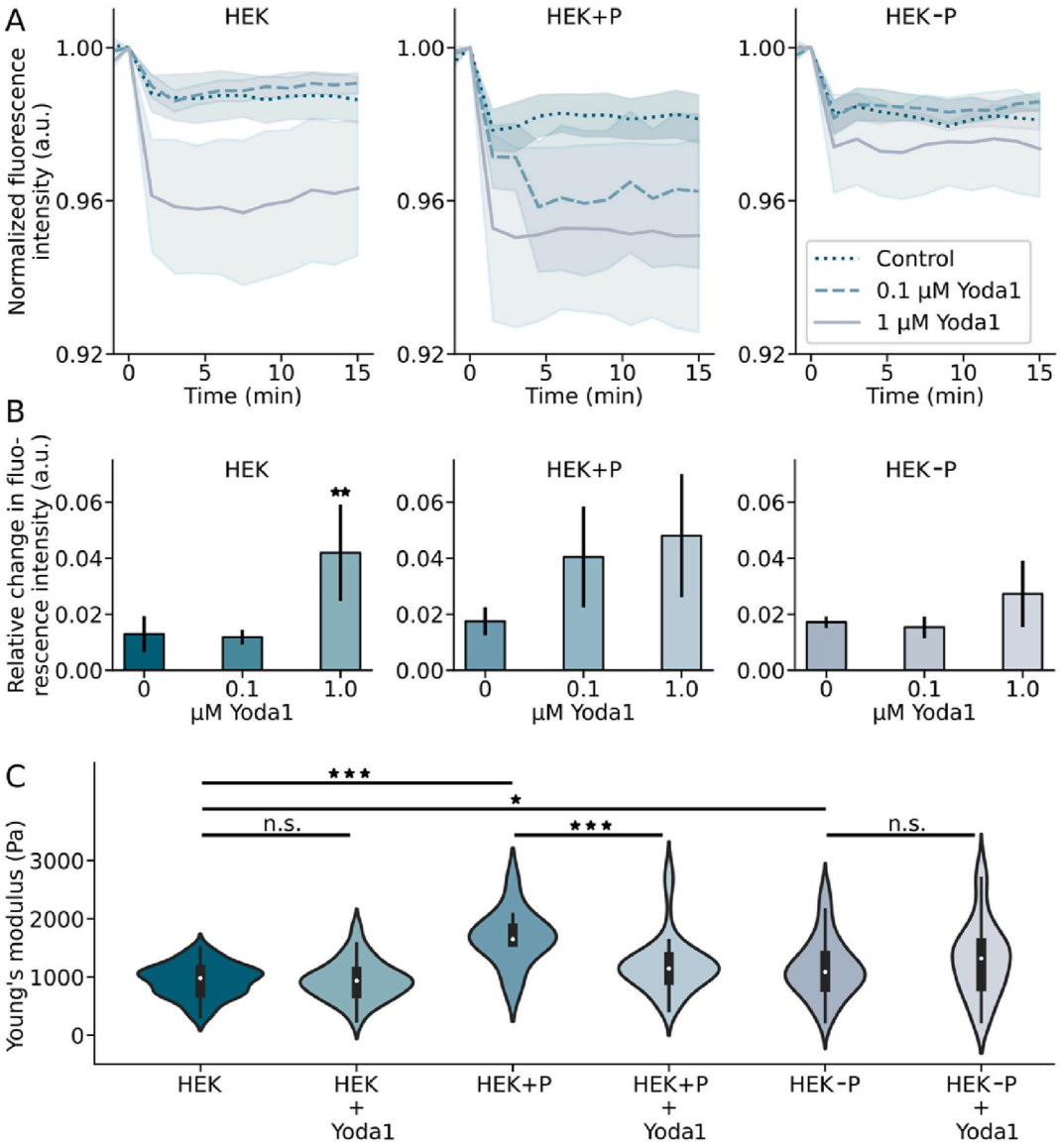

Fig. 4. Chemical activation of Piezo1 leads to an increase in the F-Actin turnover rate in HEK and HEK + P cells but decreases the stiffness only of HEK + P cells. A) Time change of SiR-Actin fluorescence signal (3 measurements at 9 positions per condition). B) Average change in fluorescence intensity between 4.5 and 7.5 min of the curves in A). C) Elasticity (Young's) modulus of cells as determined before and after the addition of 1 μM Yoda1 by nanoindentation on ≥ 100 cells per condition. For details see the methods section. *P ≤ 0.05, ***P ≤ 0.001; ns, not significant.

muted response of HEK cells could be attributed to the thin nature of the F-Actin cortex and its minor contribution to bulk stiffness.

Given the similarity in F-Actin turnover rates between HEK and HEK + P cells, the divergent stiffness behavior of Yoda1-treated HEK + P cells might indicate the presence of additional regulatory mechanisms when Piezo1 is overexpressed.

2.2.1. Piezo1 channel influences cell migration via biochemical mechanotransduction: Cofilin1

To elucidate the connection between cell migration, Piezo1, and F-Actin dynamics, we investigated the expression of Cofilin1, a protein involved in severing F-Actin microfilaments, a process essential for F-Actin depolymerization and cell migration [37,57–60]. The migration assay experiments were conducted in HEK, HEK + P, and HEK-P cells under steady-state conditions and in the presence of 2 μM Yoda1 (Fig. 5; Fig. S4).

We found distinct expressions of dephosphorylated (active form) and phosphorylated (inactive form) Cofilin1 in HEK, HEK + P, and HEK-P cells (Fig. 5A and B; Figs. S4A–S4C). This difference primarily stemmed from the Cofilin1/phosphorylated Cofilin1 (pCofilin1) ratio which gives a direct measure of the active Cofilin1 and was ~1.4 fold higher in HEK + P and ~1.6 lower in HEK-P cells when compared to control cells (Fig. 5B), indicating that Cofilin1 is more active in HEK + P and HEK compared to HEK-P cells.

The above-observed Cofilin1 expression trend was confirmed in HEK cells treated with Yoda1 (Fig. 5C and D; Figs. S4D–S4F). The

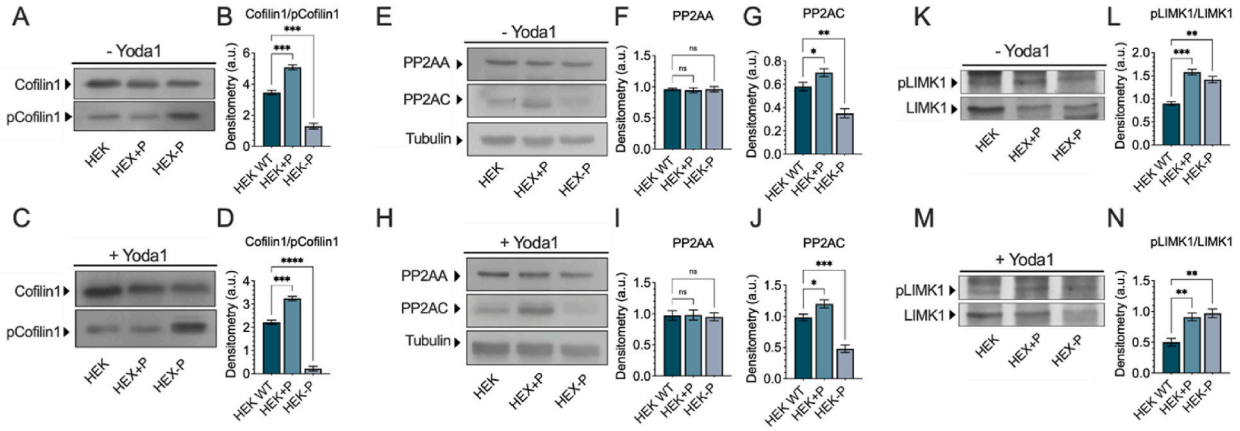

Fig. 5. Expression of Cofilin1 and PP2A in HEK, HEK + P, and HEK-P in the presence and absence of Yoda1. The same amount of proteins was separated by SDS-PAGE and Western Blotting. Densitometry analyses (a.u., arbitrary units) of protein immunostaining were conducted by the FIJI software (Fiji Life Line version 2.0.0, 2018; imagej.net [52]). Unprocessed images of Western blotting were in the supplementary material. Results are expressed as mean ± SD of three independent experiments. See also Supplementary Fig. S4 for Cofilin1 and pCofilin1 densitometric analysis by using actin as a reference. *P ≤ 0.05; **P ≤ 0.01; ****P ≤ 0.001; ns, not significant.

Cofilin1/pCofilin1 ratio was approximately 1.5-fold higher in Yoda1-treated HEK + P cells than in Yoda1-treated HEK cells, and both were higher compared to Yoda1-treated HEK-P cells (Fig. 5D).

2.3. Piezo1 channel influences cell migration via mechanotransduction: the involvement of PP2A

To delve deeper into the mechanism linking Piezo1 and Cofilin1 activation, we examined the expression of serine/threonine-protein phosphatase 2A (PP2A), the enzyme that is recognized to catalyze the dephosphorylation of Cofilin1, and its activity is downstream of Piezo1 [43,61,62].

The results showed that the higher Cofilin1 dephosphorylation by PP2A occurred in HEK + P and HEK cells (Fig. 5E–J), concurrently with the highest expression ratio of Cofilin1/pCofilin1. More in detail, the expression of the structural A subunit of PP2A (PP2AA) was similar in HEK, HEK + P, and HEK-P cells (Fig. 5E and F), while the catalytic C subunit of PP2A (PP2AC) was higher in HEK + P (>20 %) and reduced in HEK-P (<50 %) compared to HEK cells (Fig. 5E and G). This trend in both subunit expressions persisted following Yoda1 treatment of HEK, HEK + P, and HEK-P cells (Fig. 5H–J).

We also examined the expression of LIM domain kinase 1 (LIMK1) that catalyzes the phosphorylation of Cofilin1 [45,46] to explore its potential contribution to the mechanism. We observed a similar increase in the ratio of phosphorylated (p)LIMK1/LIMK1 in HEK + P and HEK-P compared to the HEK control cells, both in the presence (Fig. 5K and L) and absence of Yoda1 (Fig. 5M and N). These results suggest that LIMK1 may not be involved in the pathway downstream of Piezo1.

Therefore, the collective data suggest that Piezo1 regulates the dephosphorylation of Cofilin1 via PP2AC.

To confirm the mechanism, we investigated the impact of inhibiting PP2AC through hsa-miR-133b transfection on cell migration (Fig. 6A–C).

We applied three prediction tools, miRDB [63], RNA22 [64], and TarPmiR [65], to predict reliable microRNA (miRNA) for the target PP2AC mRNA.

First, we generated a list of predicted putative miRNA for the PPP2AC searching by gene target in the miRDB tool. The top 5 miRNAs were used for the confirmation with the other two prediction tools, RNA22 and TarPmiR (Table 1).

Table 1 showed that hsa-miR-133a-3p and hsa-miR-133b, sharing the same seed sequence, are the exclusive miR predicted by all three tools. Notably, these miRNAs are uniquely predicted to bind to the coding sequence of PP2AC mRNA, as highlighted in the RNA22 column (Table 1). Moreover, both miRNAs exhibit a minimal folding energy of about −13 kcal/mol, perfect pairing probability between the 2–7 nucleotides of miRNA with the mRNA target (seed match = 1, Table 2), the highest pairing probabilities at different positions of miRNA (m/e motif: −15.37), and the longest consecutive pairs of 11 nucleotides (Table 2) (For more details on scores please refer to Ref. [65]). Overall, the analysis suggests that hsa-miR-133b is the best candidate for specific targeting PP2AC, primarily based on its superior scores and its ability to target the 3′UTR and CDS region.

Transfection with mimic hsa-miR-133b was exclusively carried out in HEK control cells, aligning with prior experiments involving Yoda1 and GsMTx4 treatments (Fig. 2). We observed a noteworthy reduction in the PP2AC (Fig. 6A) and a diminished Cofilin1/pCofilin1 ratio in miR-transfected cells compared to Mock (cells transfected with the vehicle) and HEK untransfected cells, where the expression remained similar (Fig. 6B). Notably, there was a significant slowing-down in cell migration in miR-transfected cells, with only a ~40 % closed area compared to approximately ~70 % in CTR and Mock cells at 36 h of treatment (Fig. 6C and D).

No difference in the percentage of the closing scratched area was observed in HEK cells transfected with the miR-133b inhibitor compared to untransfected cells (Fig. S5). These findings are supported by the effect of Calyculin A 5 nM, the specific inhibitor of PP2AC in HEK cells (Fig. 6E; Fig. S6) demonstrating that after 36 h of scratching, the closed area in Calyculin A-treated cells was only

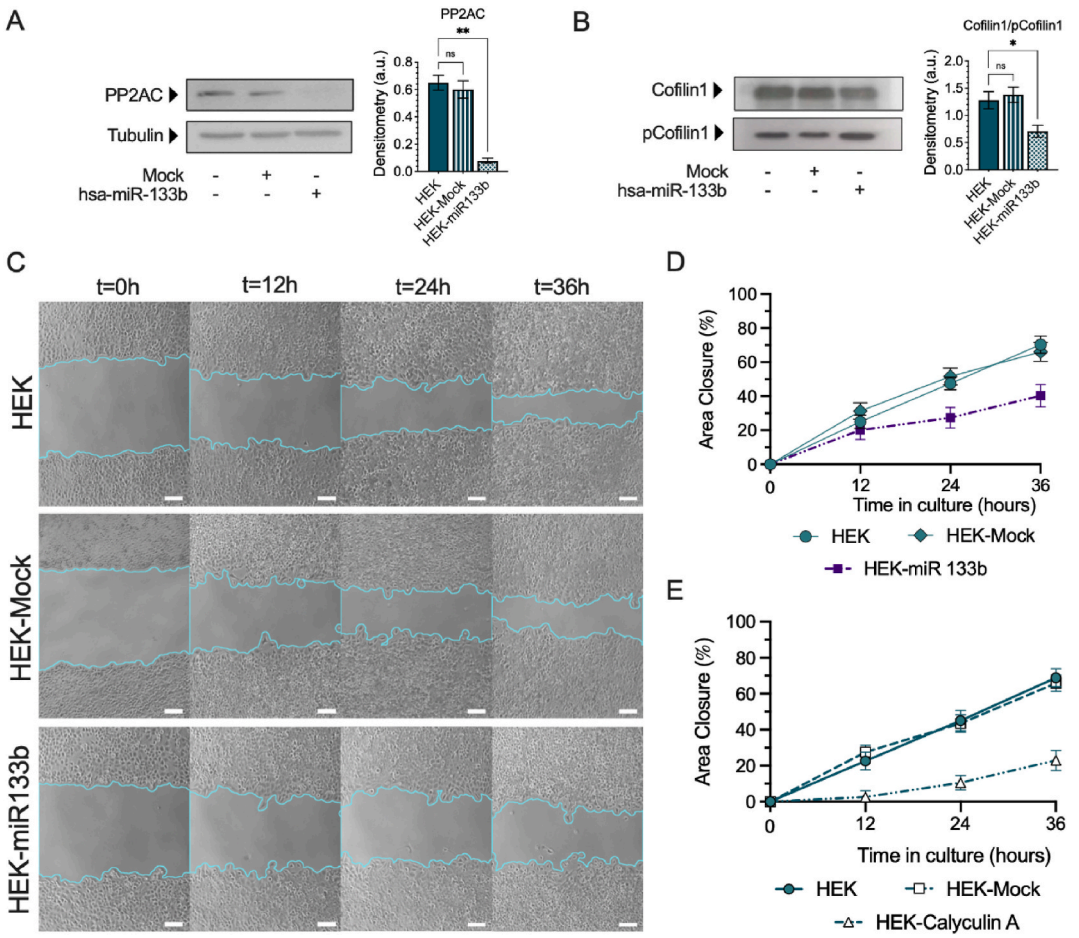

Fig. 6. Role of PP2A in migration mechanisms. A,B) Expression of PP2A subunit C (A) and expression of Cofilin1 (B) after miR-133b transfection. The same amount of proteins was separated by SDS-PAGE and Western Blotting. Densitometry analysis of protein immunostaining was conducted using the Fiji software (Fiji Life Line version 2.0.0, 2018; imagej.net [52]). Unprocessed images of Western blotting were in the supplementary material. Results are expressed as mean ± SD of three independent experiments. *P ≤ 0.05; **P ≤ 0.01; ns, not significant. C) Representative phase-contrast microscopy images of cell migration in a scratch assay in HEK cells treated with miR-133b mimic. Scale bar 100 μm. D,E) The area of each scratch (delimited by cyan lines) was measured for all images using the wound healing size tool [51], an image J plugin for the high throughput image analysis of in vitro scratch (Fiji Life Line version 2.0.0, 2018; imagej.net [52]). Representative phase-contrast microscopy images of cell migration scratch assay for graphs E are reported in Fig. S6. (For interpretation of the references to colour in this figure legend, the reader is referred to the Web version of this article.)

Table 1
miRNA against PP2AC mRNA prediction scores.

miR (miRBase ID)	miRDB score[a]	RNA22[b]	TarPmiR (m/e)[c]
has-miR-1283 (MIMAT0005799)	98	NA	−13.82
has-miR-133a-3p (MIMAT0000427)	97	−18.00	−15.37
has-miR-133b (MIMAT0000770)	97	−18.00	−15.37
has-miR-570-3p (MIMAT0003235)	97	NA	−14.47
has-miR-6730-3p (MIMAT0027362)	97	NA	−10.31

[a] Predicted score based on miRNA target sites in the 3′ untranslated regions (UTRs).
[b] Predicted score based on sequence complementarity between miRNAs and 5′UTR, target coding sequence (CDS) and 3′UTR.
[c] Support vector machine predicted score of miRNA target sites based on sequence complementarity and conservation.

~20 % when compared to HEK control and corresponding Mock cells at the same time point (Fig. 6E; Fig. S6).

To further substantiate these findings, additional experiments were conducted using siRNA targeting PP2AC and siRNA against Cofilin1 in HEK, HEK + P, and HEK-P cells (Fig. S7). Following a 36-h incubation with either siRNA targeting the PP2AC or siRNA against Cofilin1, a significant reduction in cell motility was observed in HEK (~30 %), and HEK + P (~40 %), compared to negative

Table 2
TarPmir scores: identification of the best miRNA against PP2AC mRNA.

miRNA	Binding site	Minimal Folding Energy	Seed match	m/e motif	Longest consecutive pairings
hsa-miR-1283	48,394,861	−9.20	0.833	−13.82	7
hsa-miR-133a-3p	198,219	−12.9	1	−15.37	11
hsa-miR-133b	198,219	−12.8	1	−15.37	11
hsa-miR 570-3p	13,931,413	−6.10	0.5	−14.47	8
hsa-miR-6730-3p	36,033,624	−15.2	0.833	−10.31	5

control transfected cells (Figs. S7A and S7B, HEK; S7C, S7D, HEK + P). Conversely, no notable changes in cell migration were noted in HEK-P after treatment with siRNA targeting the PP2AC or siRNA against Cofilin1 (Figs. S7E and S7F). Overall, these results indicate the involvement of PP2AC in cell migration.

In summary, the collective findings underscore the role of Piezo1 in regulating Cofilin1/severing F-Actin through the involvement of PP2AC, consequently influencing cell migration in HEK.

3. Discussion

In this study, we discovered a biochemical mechanotransduction mechanism wherein Piezo1 triggers the dephosphorylation of pCofilin1 via PP2A. This leads to increased levels of active Cofilin1 and consequent F-actin depolymerization, thereby affecting cell motility.

Additionally, our study highlights the functionality of channels in cells under steady-state conditions. This finding corroborates previous research indicating the ability of Piezo1 to activate independently of external mechanical cues [44], such as traction forces generated by stress fibers within cells.

A growing research group has investigated the involvement of Piezo1 in cell migration [15,18,22,25,26,66–68].

Reports have consistently attributed a role to this channel through various mechanisms, highlighting its dual effects on both stimulating and inhibiting cell motility.

These effects differ based on the type of tissue/cell as well as physiological and pathological conditions [15,18,22,25,26,66–68]. Understanding these mechanisms is essential for elucidating the role of Piezo1, especially in scenarios where it plays a crucial role in the onset and progression of diverse diseases such as cancer.

In this context, our study, although currently focused on HEK cells, has the potential to shed light on the biochemical pathways through which Piezo1 influences cell migration.

First, we demonstrated an increase in the cell migration rate of HEK cells treated with the channel agonist Yoda1, whereas the migration rate was significantly reduced in HEK cells treated with the mechanotoxin GsMTx4. Moreover, our findings revealed rapid migration dynamics, with nearly complete closure of scratched areas within 36 h in HEK + Yoda1 cells compared to minimal changes in HEK + GsMTx4-treated cells.

These findings were further substantiated by monitoring the F-actin remodeling induced by Piezo1 activation. Our results, confirming those of previous works [44,48], revealed a clear correlation between F-actin dynamics and Piezo1 expression levels. Specifically, F-actin stress-fiber length fragmentation was more pronounced in HEK + P cells than in HEK and HEK-P cells, indicating varying rates of polymerization and depolymerization. In this context, we interpreted the negligible difference in stress fiber length fragmentation between HEK + P cells and Yoda1-treated HEK + P cells as a result of Piezo1 functionality approaching saturation. The effect of Piezo1 on cytoskeletal organization was confirmed by real-time monitoring of the F-actin remodeling process. We observed significant alterations in the mechanical properties of HEK + P cells, whereas no discernible differences were observed between HEK and HEK-P cells. Moreover, the presence of decreased stress fiber length in HEK-P cells could be related to the basic functional remodeling of cytoskeletal components within the cells, which may involve other F-actin-linking proteins [32–34].

Hence, to clarify the impact of Piezo1 on F-actin, and thereby on cell motility, we focused on the proteins involved in F-actin dynamics. Our primary focus was on Cofilin1, a protein that plays a crucial role in regulating microfilament dynamics through the polymerization/depolymerization process, a mechanism known to be influenced by calcium concentration [37,69–71]. Specifically, an increase in Ca^{2+} levels favors the dephosphorylation of Cofilin1, thereby enhancing its severing function on F-actin [69–71]. Cofilin1 possesses two actin-binding sites: one binds to both monomeric and filamentous actin, whereas the other interacts exclusively with filaments. When unphosphorylated Cofilin1 (the active form) binds to F-actin filaments, it induces a change in subunit orientation, leading to filament severing [32–34]. This process increases the number of ends available for filament elongation or shortening depending on the cellular conditions. Additionally, the interaction of Cofilin1 with monomeric actin reduces the availability of polymerization-competent actin subunits [32–34]. Phosphorylation of Cofilin1 at Ser3 by LIMK1 results in its inactivation and loss of depolymerization function [33,34,37–39]. The severing function of Cofilin1 occurs rapidly at both the barbed and pointed ends of filaments, leading to filament fragmentation and nucleation [33,34,37–39]. As mentioned in the introduction, dephosphorylation of pCofilin1 at Ser3 may be catalyzed by phosphatase proteins, such as slingshot (SSH1, SSH2, and SSH3) [40], CIN [41], and PP2A [42].

Among these phosphatases, we prioritized PP2A, as previous studies have shown it to be downstream of Piezo1 in the MDA-MB-231 breast cancer cell line [43]. PP2A functions as a heterotrimeric holoenzyme, comprising two regulatory subunits (A and B) along with a catalytic C subunit (PP2AC), and is estimated to regulate approximately 60 % of all serine/threonine phosphorylation events within cells [72].

In our study, we observed a distinct pattern of Cofilin1 expression, with the unphosphorylated active form being the most highly expressed in HEK + P cells, followed by HEK cells, and then HEK-P cells. This expression pattern correlated with increased F-actin dynamics and higher levels of PP2AC expression in HEK + P cells than in HEK and HEK-P cells. The functional role of PP2A was further clarified through post-transcriptional inhibition experiments utilizing mir-133b, which specifically targets the PP2AC mRNA. Transfection resulted in a significant reduction in the dephosphorylation of Cofilin1, leading to deceleration of the cell migration process. This effect was replicated by inhibiting PP2A using the specific inhibitor, Calyculin A. Furthermore, confirmation was obtained through post-transcriptional inhibition of either PP2AC or Cofilin1 mRNA in HEK + P, HEK-P, and HEK cells. Using anti-PP2AC siRNA, we observed a decrease in cell migration of transfected HEK + P and HEK cells, with almost no inhibition of migration observed in transfected HEK-P cells. Similarly, anti-Cofilin1 siRNA demonstrated reduced cell migration in transfected HEK + P and HEK cells, with no inhibition of cell migration in transfected HEK-P cells. Therefore, the overall findings highlight a correlation between the expression of Piezo1, dephosphorylation of Cofilin1 by PP2AC, increase in F-actin severing, and cell motility, in the order HEK + P > HEK > HEK-P. Notably, these results pioneered the correlation between Piezo1 and Cofilin1 function. In this regard, our results support previous studies correlating the regulation of Cofilin1 function with calcium influx [69–71,73].

In conclusion, our collective findings revealed a biochemical mechanotransduction mechanism connecting Piezo1 activation, Cofilin1 phosphorylation/dephosphorylation, F-actin dynamics, and cell migration. In this regard our findings open new avenues for identifying novel therapeutic targets for diseases characterized by dysregulated cytoskeletal dynamics and disrupted cell migration. However, due to the above discussed dual effects on both stimulating and inhibiting cell motility, additional research is necessary to understand whether Piezo1 influences cell motility in other tissues and cells by the suggested biochemical mechanotransduction mechanism.

4. Materials and methods

4.1. HEK293T cells model for Piezo1 overexpression and knockout

HEK293T cells overexpressing Piezo1 (HEK + P), and HEK293T cells Piezo1 knockout (HEK-P) were generated from the HEK293T (HEK) cell line (ATCC; https://www.atcc.org) and kindly provided by Prof. B. Martinac and Dr. C. Cox from Victor Chang Cardiac Research Institute, Sydney, Australia [26,47,48]. Engineered and wild-type cells were cultured in tissue culture polystyrene flasks (TCP) in the growth culture medium (DMEM High Glucose (Euroclone S.p.A, Pero (MI), Italy) supplemented with 10 % Fetal Bovine Serum (FBS, Euroclone S.p.A, Pero (MI), Italy), 1 % penicillin–streptomycin (Euroclone S.p.A, Pero (MI), Italy) and 2 mM L-glutamine (Euroclone S.p.A, Pero (MI), Italy) in a humidified atmosphere and 5 % of CO2 at 37 °C. Every three days, the culture medium was changed.

Cells were seeded on glass slides coated with poly-D-lysine, at about 10 % confluence for 16–20 h for super-resolution imaging, at about 50 % confluence for 2 days for SiR-Actin imaging and the micropipette assay, and at 100 % confluence for 2 days for nano-indentation experiments.

4.2. Cell viability

The viability of HEK, HEK + P, and HEK-P cells cultured in growth culture medium at the starting concentration of 3.0×10^3 cells/mL was determined at different times, 1, 2, 3, 4, 7, and 14 days (D) using the MTT (3-(4,5-dimethylthiazol-2-yl)-2,5-diphenyltetrazolium bromide) (Sigma Aldrich, St. Louis, MI, USA) assay, performed according to the manufacturer's recommendations. Using a microtiter plate reader (ELISA reader, DV990BV6, GDV, Roma, Italy), the absorbance was measured at 589 nm with a reference wavelength of 650 nm. The data are reported as the mean ± SD of three independent experiments.

4.3. Cell proliferation

A growth curve for HEK, HEK + P, and HEK-P cells was generated by seeding 3.0×10^3 cells into 12-multiwell plates in growth culture medium and counting at various time points (D1, D2, D3, D4, D7, and D21). First, all cell types were synchronized overnight by removing the FBS in the culture medium. Each experiment was conducted twice for each cell type. Following trypsinization, the pellet was resuspended in PBS and the cell suspension was mixed with Trypan Blue solution for counting. The cell counting was performed by using the Invitrogen™ Counteness™ automated cell counter (Invitrogen™, Grand Island, NY, USA) according to the recommended procedure.

Cell doubling time was calculated according to Eq. (1):

$$Doubling\ time = \left(\frac{T\ x\ ln\ 2}{ln(Cf/Ci)}\right) \quad \text{(Eq. 1)}$$

where T = Time in hour; C_f = number of cells at the end of T; C_i = number of cells at T0.

4.4. BrdU assay

The BrDU proliferation assay was conducted using the EdU Click-iT cell proliferation kit (Invitrogen™, Grand Island, NY, USA)

following the manufacturer's specifications (Invitrogen™, Grand Island, NY, USA). Briefly, 1.5×10^3 of HEK, HEK + P, and HEK-P cells were seeded on glass coverslips previously sterilized in 70 % Et-OH and placed in a 24 multiwell. Each well was treated with a 20 μM concentration of 5-bromo-2′-deoxyuridine, and the cells were cultured for 3, 6, 9, and 15 h, respectively. After the designated incubation period with BrdU, the cells were fixed with 4 % paraformaldehyde (20 min), incubated with permeabilization solution (PBS+3 % FBS+0.5 % Triton X-100), and then each well was incubated with the "Click-it Reaction Cocktails" containing the Alexa Fluor-488. Glass coverslips were mounted with Vectashield Antifade Mounting Medium with DAPI (Vector Laboratories Inc., Burlingame, CA, USA) and the proliferation was evaluated using a fluorescence microscope (Eclipse-TE2000-S, Nikon, Tokyo, Japan) equipped with the F-ViewII FireWire camera and Cell^f software (Soft Imaging System, Olympus, Münster, Germany, version 2.5, Accessed in 2006). The dividing nuclei were depicted in GREEN, while the total number of nuclei was visible in BLUE. Following the counting of nuclei (10 photos for each glass coverslip), we calculated the percentage of S-phase cells relative to the total number of cells. The results are expressed as mean of three independent experiments mean ± standard deviation (SD).

4.5. Treatment of cells with Yoda1, GsMTx4, and Calyculin A

To activate the channel Piezo1 all three types of cells used were incubated with the specific activator Yoda1 (Sigma-Aldrich, St. Louis, MO, USA). Yoda1 was dissolved in DMSO at the stock concentration of 1 mM and utilized at a final concentration of 0.1–2 μM in the growth medium. For F-Actin staining and western blotting, Yoda1 was incubated for 10 min while for the migration assay, Yoda1 was added to the culture medium at T0 and T6.

To inhibit the channel Piezo1 in HEK cells GsMTx4 was employed *(*Tocris Bioscience, Bristol, UK*)*. GsMTx4 was dissolved in distilled water at the stock concentration of 244 μM and used at the final concentration of 4 μM in the culture medium. For the migration assay, GsMTx4 was added to the medium at T0 and T6.

To inhibit the activity of PP2A Calyculin A (Cell Signaling Technology, Danvers, MA, USA) was used. Calyculin A was dissolved in DMSO at the stock concentration of 50 mM and used at the final concentration of 5 nM. For the migration assay, Calyculin A was added to the medium at T0 and T12.

4.6. Selection of has-miR-133b

The selection of microRNA (miR) was conducted using bioinformatics tools designed to predict miRNA target interactions. Specifically, three prediction tools, miRDB [63], RNA22 [64], and TarPmiR [65] were employed to predict reliable miRNAs for the target PP2AC. While these tools share a common goal, they are different in their algorithms, features, and performance. miRDB (microRNA target prediction and functional annotation database) is a web-based tool that predicts miRNA target genes based on sequence complementarity between miRNAs and target mRNAs; RNA22 is a computational tool specifically designed for predicting miRNA target sites in the 3′ untranslated regions (UTRs) of mRNAs; TarPmiR (Target Prediction for miRNA) is another web-based tool used for predicting miRNA targets. It uses a support vector machine (SVM) algorithm to predict miRNA target sites based on sequence complementarity and conservation. TarPmiR incorporates various features, such as seed region match, local RNA structure, and thermodynamic stability, to improve target prediction accuracy.

Optimal selection of miRNA-specific targets was achieved when all three tools yielded overlapping results.

4.7. hsa-miR-133b cell transfection

Cells were transiently transfected with hsa-miR-133b mimic 50 nM (miRIDIAN microRNA Mimic, Dharmacon cod: C-300709-07-0050) or with hsa-miR-133b mimic inhibitor 50 nM (miRIDIAN microRNA Hairpin Inhibitor, Dharmacon cod: IH-300709-06-0050) in Lipofectamine™ 3000 Transfection Reagent (Invitrogen, Grand Island, NY, USA) according to manufacturer's instructions. Mock control (Lipofectamine™ 3000 Transfection Reagent without has-miR-133b), and untransfected cells were used as reference. The procedure was carried out in triplicate on a 24-well plate, where 5×10^5 HEK cells were seeded on TCP in a volume of 500 μL of growth medium. Considering the cell's duplication time, cells were subjected to a second transfection round at 18 h under the same experimental conditions.

4.8. siRNA cell transfection

The PP2A-C siRNA(h) (sc-43509), Cofilin 1 siRNA (h) (sc-35078), and control siRNA (sc-37007) were purchased from Santa Cruz Biotechnology. Cells were transfected by LipofectamineRNAiMAX (Invitrogen, Grand Island, NY, USA) according to the manufacturer's instructions. The procedure was carried out in triplicate on a 24-well plate, where 5×10^5 HEK cells were seeded on TCP in a volume of 500 μL of growth medium. Considering the cell's duplication time, cells were subjected to a second transfection round at 18 h under the same experimental conditions.

4.9. Migration assay

The suspension (3×10^6 cells/mL) of each cell line HEK, HEK + P, and HEK-P were seeded in a well plate and incubated for 12 h in DMEM media without FBS to establish a confluent monolayer and synchronize the culture. A straight line was created by scratching the monolayer cells with a sterile P200 pipe tip. After the scratch to remove the detached cells, the cultures were rinsed with PBS, and then

was added growth culture medium (untreated control cells) or the culture medium enriched with 2 μM of Yoda1, or 4 μM of GsMTx4 (treated cells), or with hsa-miR-133b mimic, hsa-miR-133b inhibitor, PP2A-C siRNA Cofilin 1 siRNA, or Calyculin A, and related controls. The size of the scratches in untreated and treated cells was measured using the microscope Eclipse-TE2000-S Nikon microscope (Nikon, Düsseldorf, Germany).

The ability of the cells to migrate was evaluated at time points of 0 h (t = 0 h), 24 h (t = 24 h), 48 h (t = 48 h), and 72 h (t = 72 h) to confirm the differences in HEK, HEK + P, and HEK-P cell migration observed in previous work; at 0 h (t = 0 h), 2 h (t = 2 h), 4 h (t = 4 h), 6 h (t = 6 h), 12 h (t = 12 h), 24 h (t = 24 h), 36 h (t = 36 h), after the scratch for the cells untreated and treated with GsMTx4 and Yoda1; at 0 h (t = 0 h), 12 h (t = 12 h), 24 h (t = 24 h), 36 h (t = 36 h) following the scratch for the cells untreated and treated with hsa-miR-133b and Calyculin A. At each time point, the scratch images were captured with a digital camera PowerShot G10, Canon (PowerShot G10, Canon, Tokyo, Japan) and brightfield microscopy Eclipse-TE2000-S, Nikon (Nikon, Düsseldorf, Germany). The area of each scratch was measured for all images using the wound healing size tool, an image J plugin for the high throughput image analysis of in vitro scratch with FIJI (FIJI Life Line version 2.0.0, 2018; imagej.net). Each experiment was performed in triplicate.

The measurements of the closing area and the migration rate are calculated from the image quantification according to Eq. (1) and Eq. (2), respectively:

$$Area\ Closure\ (\%) = \left(\frac{A_{t=0} - A_{t=\Delta t}}{A_{t=0}}\right) x100 \quad \text{(Eq. 1)}$$

where $A_{t=0}$ is the initial aperture area (μm^2) at t = 0 h, $A_{t=\Delta t}$ is the aperture area (μm^2) after n hours from the initial scratch;

$$Migration\ Rate\ (\mu m) = \frac{W_i - W_f}{t} \quad \text{(Eq. 2)}$$

where W_i is the average of the initial scratch width (μm), W_f is the average of the final scratch width (μm) and t (hours) is the time of the assay.

4.10. Cell extract and protein quantification

According to our procedures, HEK, HEK + P, and HEK-P cells were harvested, and washed in PBS, and the cell pellet was subsequently resuspended in sodium phosphate buffer (10 mM, pH 6.0) containing 0.1 % (v/v) Nonidet NP40 detergent (Sigma-Aldrich, St. Louis, MO, USA). Three rounds of sonication were then performed (30 s each). Every procedure was conducted at 4 °C. Protein content was measured using the Bradford method, utilizing bovine serum albumin as a reference [74].

4.11. SDS-PAGE electrophoresis and western blotting

40 μg of protein extract were analyzed by SDS-PAGE electrophoresis and Western blotting, according to our work [75]. The antigen detection was conducted with the primary antibodies by incubation overnight at 4 °C and with the secondary antibody by incubation for 1 h at room temperature (RT) (see Table 3 for antibodies list). The immunodetection was performed using the Clarity™ Western ECL Blotting Substrate (GE Healthcare, Fairfield, CT, USA). The same blotting membrane was re-probed with different primary antibodies for comparative analyses. Densitometry analyses of protein immunostaining were conducted by the FIJI software (FIJI Life Line version 2.0.0, 2018; imagej.net) [52]. Relative band intensities were standardized to Actin as a reference. Results are expressed as mean ± SD of three independent experiments.

4.12. Immunofluorescences

Immunofluorescences were conducted as previously described [75–77]. In brief, 1×10^3 of HEK, HEK + P, and HEK-P cells seeded on glass coverslips in 24 well plates and were fixed with 4 % paraformaldehyde, were incubated with permeabilization solution (PBS+3 % FBS+0.5 % Triton X-100) and then in blocking solution (PBS+3 % FBS+0.05 % Triton X-100) for 1 h at RT. Cells on glass

Table 3
Antibodies list.

Antibody	Source	Dilution
anti-Piezo1	Novus Biologicals, Centennial, Colorado, USA	1:50
anti-rabbit IgG, HRP-linked Antibody	Cell Signaling Technology, Danvers, MA, USA	1:15000
anti-mouse IgG, HRP-linked Antibody	Cell Signaling Technology, Danvers, MA, USA	1:15000
anti-pCofilin1 Ser3	Elabscience, Houston, TX, USA	1:1000
anti-Cofilin1	Santa Cruz Biotechnology, CA, USA	1:200
anti-Vinculin	Abcam, Cambridge, UK	1:100
anti-PP2A_SubC	Cell Signaling Technology, Danvers, MA, USA	1:1000
anti-PP2A_SubA	Cell Signaling Technology, Danvers, MA, USA	1:1000
anti-LIMK1	Santa Cruz Biotechnology, CA, USA	1:1000
anti-pLIMK1	Cell Signaling Technology, Danvers, MA, USA	1:500

coverslips were incubated with the primary antibody overnight at 4 °C and then with the related secondary antibody (Donkey anti-Rabbit) conjugated with Alexa-Fluor-594 (Invitrogen™, Grand Island, NY, USA) for 1 h at RT. In some experiments, the F-Actin was stained by incubating the cells with Phalloidin (Alexa-fluor-488 phalloidin, Invitrogen™, Grand Island, NY, USA) for 20 min at RT.

Glass coverslips were mounted and nuclei counterstained with Vectashield mounting medium with DAPI (Vector Laboratories Inc., Burlingame, CA, USA). As a negative control, cells on a glass coverslip were incubated only with the above-indicated conjugated secondary antibodies.

Images were acquired with fluorescence microscopy (Eclipse-TE2000-S, Nikon, Tokyo, Japan) using the F-ViewII FireWire camera (cell^f Soft Imaging System, Olympus, Germany, version 2.5, Accessed in 2006).

4.13. Computational images quantification

For each cell sample (HEK, HEK + P, and HEK-P cells), 50 stained cells were acquired with fluorescence microscopy (Eclipse-TE2000-S, Nikon) and evaluated. Before quantification, some enhancement operations were performed on each image: (i) non-uniform illumination correction, with a Gaussian smoothing filter, was applied [imflatfield function implemented in MatLab (MathWorks, Inc., Natick, MA, USA, version R2019b)], and (ii) background subtraction was done, applying an opening morphological operation, using a disk of 20-pixel diameter [imopen function implemented in Matlab (MathWorks, Inc., Natick, MA, USA, version R2019b)]. Finally, each image was thresholded, cells were masked, and the region properties (area, perimeter, and hull convex area) of the masked region of interest (ROI) were calculated.

The Cell Spread Area (CSA) was obtained from the equation:

$$CSA = \mathrm{N} * \mathrm{px}^2$$

where N = number of foreground pixels in the mask, px = pixel size in microns, px^2 = converts the pixel size to micron^2 to give the area per pixel.

The Cellular Shape Index (CSI) was obtained from the relationship:

$$CSI = \frac{4 \times \pi \times \mathrm{A}}{p^2}$$

where:

A = cell area

p = perimeter of the cell.

A value of 1 indicated a perfect circle, whereas a value approaching zero indicates an increasingly longer, narrower, and more protruded morphology.

The Solidity was obtained from the relationship:

$$Solidity = \frac{\mathrm{A_c}}{\mathrm{A}_h}$$

where:

A_c = cell area

A_h = convex hull area

Solidity is a parameter of cells with protrusions or irregular shapes than round-shaped cells.

The architectures of Actin fiber networks were segmented and quantified from fluorescence images by using the open-source MATLAB package Stress Fiber Extractor [SFEX] [54].

4.14. Actin polymerization assay

The Actin polymerization rate was determined as reported previously [55] by staining cells with 100 nM SiR F-Actin (Spirochrome, Stein am Rhein, Switzerland) for 12–18 h, and performing time-lapse imaging on an FV3000 confocal microscope (Olympus Life Science, Waltham, USA) with automatic focus control at 37 °C in physiological solution. Average fluorescent intensities were extracted from the images by a custom Python script using thresholding.

4.15. Nanoindentation

Nanoindentation measurements were performed with a FluidFM system as described previously [56]. Briefly, the system was composed of a Flex-AFM (Nanosurf AG, Liestal, Switzerland), a pressure controller (Cytosurge AG, Opfikon, Switzerland), and a tipless FluidFM probe with a 2 μm circular aperture and 0.3 N/m spring constant, that was filled with PBS and calibrated with the standard methods. By applying negative pressure, colloids with a 5 μm diameter were attached to the cantilever aperture. Subsequently, force spectroscopy was performed on confluent cell layers in a physiological solution at 37 °C in grids of 5 × 5 points separated by 25 μm with an approach speed of 1 μm/s and a stop value of 10 nN. The cell stiffness was extracted from the force curves by fitting the Hertz function as described previously [56].

4.16. Statistical analyses

Data are reported as the mean ± SD of results from three independent experiments. A post-hoc comparison test was performed by the one-way ANOVA and Dunnett's multiple comparison test with respect to the WT control group (GraphPad 8.0 Software, San Diego, California, USA). $P \leq 0.05$ was considered statistically significant.

Data availability statement

Data will be made available on request.

CRediT authorship contribution statement

Francesco Morena: Writing – review & editing, Software, Methodology, Investigation, Formal analysis, Data curation, Conceptualization. **Chiara Argentati:** Methodology, Investigation. **Silvia Caponi:** Investigation, Funding acquisition. **Ines Lüchtefeld:** Investigation, Funding acquisition. **Carla Emiliani:** Funding acquisition. **Massimo Vassalli:** Conceptualization. **Sabata Martino:** Writing – review & editing, Writing – original draft, Supervision, Funding acquisition, Formal analysis, Conceptualization.

Declaration of competing interest

The authors declare that they have no known competing financial interests or personal relationships that could have appeared to influence the work reported in this paper.

Acknowledgments

This work has been funded by the European Union - NextGenerationEU under the Italian Ministry of University and Research (MUR) National Innovation Ecosystem grant ECS00000041 - VITALITY. We acknowledge Università degli Studi di Perugia and MUR for support within the project Vitality. I.L. acknowledges the funding from the EUREKA Network (Eurostars Project E!11644 SOUL).

Appendix A. Supplementary data

Supplementary data to this article can be found online at https://doi.org/10.1016/j.heliyon.2024.e32458.

References

[1] P. Ridone, M. Vassalli, B. Martinac, Piezo1 mechanosensitive channels: what are they and why are they important, Biophys. Rev. 11 (2019) 795–805, https://doi.org/10.1007/S12551-019-00584-5.
[2] S.E. Murthy, A.E. Dubin, A. Patapoutian, Piezos thrive under pressure: mechanically activated ion channels in health and disease, Nat. Rev. Mol. Cell Biol. 18 (2017) 771–783, https://doi.org/10.1038/NRM.2017.92.
[3] Z. Zhou, X. Ma, Y. Lin, D. Cheng, N. Bavi, G.A. Secker, J.V. Li, V. Janbandhu, D.L. Sutton, H.S. Scott, et al., MyoD-family inhibitor proteins act as auxiliary subunits of Piezo channels, Science 381 (2023) 799–804, https://doi.org/10.1126/SCIENCE.ADH8190/SUPPL_FILE/SCIENCE.ADH8190_SM.PDF.
[4] I. Tortorella, C. Argentati, C. Emiliani, F. Morena, S. Martino, Biochemical pathways of cellular mechanosensing/mechanotransduction and their role in neurodegenerative diseases pathogenesis, Cells 11 (2022) 3093, https://doi.org/10.3390/CELLS11193093. **2022**, *11*, 3093.
[5] I. Tortorella, C. Argentati, C. Emiliani, S. Martino, F. Morena, The role of physical cues in the development of stem cell-derived organoids, Eur. Biophys. J. 51 (2022) 105–117, https://doi.org/10.1007/S00249-021-01551-3.
[6] J. Ge, W. Li, Q. Zhao, N. Li, M. Chen, P. Zhi, R. Li, N. Gao, B. Xiao, M. Yang, Architecture of the mammalian mechanosensitive Piezo1 channel, Nature 527 (2015) 64–69, https://doi.org/10.1038/NATURE15247.
[7] X.Z. Fang, T. Zhou, J.Q. Xu, Y.X. Wang, M.M. Sun, Y.J. He, S.W. Pan, W. Xiong, Z.K. Peng, X.H. Gao, et al., Structure, kinetic properties and biological function of mechanosensitive Piezo channels, Cell Biosci. 11 (2021) 1–20, https://doi.org/10.1186/S13578-020-00522-Z, 111 2021.
[8] S.M. Cahalan, V. Lukacs, S.S. Ranade, S. Chien, M. Bandell, A. Patapoutian, Piezo1 links mechanical forces to red blood cell volume, Elife 4 (2015), https://doi.org/10.7554/ELIFE.07370.
[9] M.M. Pathak, J.L. Nourse, T. Tran, J. Hwe, J. Arulmoli, D.T.T. Le, E. Bernardis, L.A. Flanagan, F. Tombola, Stretch-activated ion channel Piezo1 directs lineage choice in human neural stem cells, Proc. Natl. Acad. Sci. U.S.A. 111 (2014) 16148–16153, https://doi.org/10.1073/PNAS.1409802111.
[10] Y. Song, D. Li, O. Farrelly, L. Miles, F. Li, S.E. Kim, T.Y. Lo, F. Wang, T. Li, K.L. Thompson-Peer, et al., The mechanosensitive ion channel Piezo inhibits axon regeneration, Neuron 102 (2019) 373, https://doi.org/10.1016/J.NEURON.2019.01.050.
[11] W. Sun, S. Chi, Y. Li, S. Ling, Y. Tan, Y. Xu, F. Jiang, J. Li, C. Liu, G. Zhong, et al., The mechanosensitive Piezo1 channel is required for bone formation, Elife 8 (2019), https://doi.org/10.7554/ELIFE.47454.
[12] K. Saotome, S.E. Murthy, J.M. Kefauver, T. Whitwam, A. Patapoutian, A.B. Ward, Structure of the mechanically activated ion channel Piezo1, Nature 554 (2018) 481–486, https://doi.org/10.1038/NATURE25453.
[13] S.L. Alper, Genetic diseases of PIEZO1 and PIEZO2 dysfunction, Curr. Top. Membr. 79 (2017) 97–134, https://doi.org/10.1016/BS.CTM.2017.01.001.
[14] P.L. Moura, B.R. Hawley, J.G.G. Dobbe, G.J. Streekstra, M.A.E. Rab, P. Bianchi, R. Van Wijk, A.M. Toye, T.J. Satchwell, PIEZO1 gain-of-function mutations delay reticulocyte maturation in hereditary xerocytosis, Haematologica 105 (2020) E268–E271, https://doi.org/10.3324/HAEMATOL.2019.231159.
[15] Y. Yu, X. Wu, S. Liu, H. Zhao, B. Li, H. Zhao, X. Feng, Piezo1 regulates migration and invasion of breast cancer cells via modulating cell mechanobiological properties, Acta Biochim. Biophys. Sin. 53 (2021) 10–18, https://doi.org/10.1093/ABBS/GMAA112.
[16] X. Chen, S. Wanggou, A. Bodalia, M. Zhu, W. Dong, J.J. Fan, W.C. Yin, H.K. Min, M. Hu, D. Draghici, et al., A feedforward mechanism mediated by mechanosensitive ion channel Piezo1 and tissue mechanics promotes glioma aggression, Neuron 100 (2018) 799–815.e7, https://doi.org/10.1016/J.NEURON.2018.09.046.

[17] L. Gao, Y. Ji, L. Wang, M. He, X. Yang, Y. Qiu, X. Sun, Z. Ji, G. Yang, J. Zhang, et al., Suppression of esophageal squamous cell carcinoma development by mechanosensitive protein Piezo1 downregulation, ACS Omega 6 (2021) 10196–10206, https://doi.org/10.1021/ACSOMEGA.1C00505/SUPPL_FILE/AO1C00505_SI_001.PDF.

[18] X. Wang, G. Cheng, Y. Miao, F. Qiu, L. Bai, Z. Gao, Y. Huang, L. Dong, X. Niu, X. Wang, et al., Piezo type mechanosensitive ion channel component 1 facilitates gastric cancer omentum metastasis, J. Cell Mol. Med. 25 (2021) 2238–2253, https://doi.org/10.1111/JCMM.16217.

[19] M. Velasco-Estevez, N. Koch, I. Klejbor, F. Caratis, A. Rutkowska, Mechanoreceptor Piezo1 is downregulated in multiple Sclerosis brain and is involved in the maturation and migration of oligodendrocytes in vitro, Front. Cell. Neurosci. 16 (2022), https://doi.org/10.3389/FNCEL.2022.914985.

[20] Z. Huang, Z. Sun, X. Zhang, K. Niu, Y. Wang, J. Zheng, H. Li, Y. Liu, Loss of stretch-activated channels, PIEZOs, accelerates non-small cell lung cancer progression and cell migration, Biosci. Rep. 39 (2019), https://doi.org/10.1042/BSR20181679.

[21] V.I. Chubinskiy-Nadezhdin, V.Y. Vasileva, I.O. Vassilieva, A.V. Sudarikova, E.A. Morachevskaya, Y.A. Negulyaev, Agonist-induced Piezo1 activation suppresses migration of transformed fibroblasts, Biochem. Biophys. Res. Commun. 514 (2019) 173–179, https://doi.org/10.1016/J.BBRC.2019.04.139.

[22] J.R. Holt, W.Z. Zeng, E.L. Evans, S.H. Woo, S. Ma, H. Abuwarda, M. Loud, A. Patapoutian, M.M. Pathak, Spatiotemporal dynamics of PIEZO1 localization controls keratinocyte migration during wound healing, Elife 10 (2021), https://doi.org/10.7554/ELIFE.65415.

[23] C.S.C. Liu, T. Mandal, P. Biswas, M.A. Hoque, P. Bandopadhyay, B.P. Sinha, J. Sarif, R. D'Rozario, D.K. Sinha, B. Sinha, et al., Piezo1 mechanosensing regulates integrin-dependent chemotactic migration in human T cells, Elife 12 (2024), https://doi.org/10.7554/ELIFE.91903.2.

[24] S.P. Wang, B. Wang, Y. Shi, T. Möller, R.I. Stegmeyer, B. Strilic, T. Li, Z. Yuan, C. Wang, N. Wettschureck, et al., Mechanosensation by endothelial PIEZO1 is required for leukocyte diapedesis, Blood 140 (2022) 171–183, https://doi.org/10.1182/BLOOD.2021014614.

[25] F. Mousawi, H. Peng, J. Li, S. Ponnambalam, S. Roger, H. Zhao, X. Yang, L.H. Jiang, Chemical activation of the Piezo1 channel drives mesenchymal stem cell migration via inducing ATP release and activation of P2 receptor purinergic signaling, Stem Cell. 38 (2020) 410–421, https://doi.org/10.1002/STEM.3114.

[26] L. Sforna, A. Michelucci, F. Morena, C. Argentati, F. Franciolini, M. Vassalli, S. Martino, L. Catacuzzeno, Piezo1 Controls Cell Volume and Migration by Modulating Swelling-Activated Chloride Current through Ca2+ Influx, vol. 237, 2022, pp. 1857–1870, https://doi.org/10.1002/JCP.30656.

[27] S. SenGupta, C.A. Parent, J.E. Bear, The principles of directed cell migration, Nat. Rev. Mol. Cell Biol. 22 (2021) 529–547, https://doi.org/10.1038/S41580-021-00366-6.

[28] L. Blanchoin, R. Boujemaa-Paterski, C. Sykes, J. Plastino, Actin dynamics, architecture, and mechanics in cell motility, Physiol. Rev. 94 (2014) 235–263, https://doi.org/10.1152/PHYSREV.00018.2013.

[29] S. Seetharaman, S. Etienne-Manneville, Cytoskeletal crosstalk in cell migration, Trends Cell Biol. 30 (2020) 720–735, https://doi.org/10.1016/J.TCB.2020.06.004.

[30] D.E. Ingber, I. Tensegrity, Cell structure and hierarchical systems biology, J. Cell Sci. 116 (2003) 1157–1173, https://doi.org/10.1242/JCS.00359.

[31] T.D. Pollard, G.G. Borisy, Cellular motility driven by assembly and disassembly of actin filaments, Cell 112 (2003) 453–465, https://doi.org/10.1016/S0092-8674(03)00120-X.

[32] J.J. Bravo-Cordero, M.A.O. Magalhaes, R.J. Eddy, L. Hodgson, J. Condeelis, Functions of cofilin in cell locomotion and invasion, Nat. Rev. Mol. Cell Biol. 14 (2013) 405–417, https://doi.org/10.1038/NRM3609.

[33] S. Arber, F.A. Barbayannis, H. Hanser, C. Schnelder, C.A. Stanyon, O. Bernards, P. Caroni, Regulation of actin dynamics through phosphorylation of cofilin by LIM-kinase, Nature 393 (1998) 805–809, https://doi.org/10.1038/31729.

[34] J.N. Namme, A.K. Bepari, H. Takebayashi, Cofilin signaling in the CNS physiology and neurodegeneration, Int. J. Mol. Sci. 22 (2021), https://doi.org/10.3390/IJMS221910727.

[35] Y. Bai, F. Zhao, T. Wu, F. Chen, X. Pang, Actin polymerization and depolymerization in developing vertebrates, Front. Physiol. 14 (2023) 1213668, https://doi.org/10.3389/FPHYS.2023.1213668/BIBTEX.

[36] J.R. Bamburg, Proteins of the ADF/cofilin family: essential regulators of actin dynamics, Annu. Rev. Cell Dev. Biol. 15 (1999) 185–230, https://doi.org/10.1146/ANNUREV.CELLBIO.15.1.185.

[37] K. Mizuno, Signaling mechanisms and functional roles of cofilin phosphorylation and dephosphorylation, Cell. Signal. 25 (2013) 457–469, https://doi.org/10.1016/J.CELLSIG.2012.11.001.

[38] C. Prunier, R. Prudent, R. Kapur, K. Sadoul, L. Lafanechère, LIM kinases: cofilin and beyond, Oncotarget 8 (2017) 41749, https://doi.org/10.18632/ONCOTARGET.16978.

[39] E. Andrianantoandro, T.D. Pollard, Mechanism of actin filament turnover by severing and nucleation at different concentrations of ADF/cofilin, Mol. Cell. 24 (2006) 13–23, https://doi.org/10.1016/J.MOLCEL.2006.08.006.

[40] H. Bielig, K. Lautz, P.R. Braun, M. Menning, N. Machuy, C. Brügmann, S. Barisic, S.A. Eisler, M. Andree, B. Zurek, et al., The cofilin phosphatase slingshot homolog 1 (SSH1) links NOD1 signaling to actin remodeling, PLoS Pathog. 10 (2014), https://doi.org/10.1371/JOURNAL.PPAT.1004351.

[41] A. Gohla, J. Birkenfeld, G.M. Bokoch, Chronophin, a novel HAD-type serine protein phosphatase, regulates cofilin-dependent actin dynamics, Nat. Cell Biol. 7 (2005) 21–29, https://doi.org/10.1038/NCB1201.

[42] K. Ohashi, Roles of cofilin in development and its mechanisms of regulation, Dev. Growth Differ. 57 (2015) 275–290, https://doi.org/10.1111/DGD.12213.

[43] P. O'Callaghan, A. Engberg, O. Eriksson, N. Fatsis-Kavalopoulos, C. Stelzl, G. Sanchez, O. Idevall-Hagren, J. Kreuger, Piezo1 activation attenuates thrombin-induced blebbing in breast cancer cells, J. Cell Sci. 135 (2022), https://doi.org/10.1242/JCS.258809/VIDEO-4.

[44] J.L. Nourse, M.M. Pathak, How Cells Channel Their Stress: Interplay between Piezo1 and the Cytoskeleton, vol. 71, 2017, pp. 3–12, https://doi.org/10.1016/J.SEMCDB.2017.06.018.

[45] J. Su, Y. Zhou, Z. Pan, L. Shi, J. Yang, A. Liao, Q. Liao, Q. Su, Downregulation of LIMK1–ADF/cofilin by DADS inhibits the migration and invasion of colon cancer, Sci. Rep. 7 (2017) 1–12, https://doi.org/10.1038/srep45624, 71 2017.

[46] N. Yang, O. Higuchi, K. Ohashi, K. Nagata, A. Wada, K. Kangawa, E. Nishida, K. Mizuno, Cofilin phosphorylation by LIM-kinase 1 and its role in Rac-mediated actin reorganization, Nature 393 (1998) 809–812, https://doi.org/10.1038/31735.

[47] A.E. Dubin, S. Murthy, A.H. Lewis, L. Brosse, S.M. Cahalan, J. Grandl, B. Coste, A. Patapoutian, Endogenous Piezo1 can confound mechanically activated channel identification and characterization, Neuron 94 (2017) 266–270.e3, https://doi.org/10.1016/J.NEURON.2017.03.039.

[48] C.D. Cox, C. Bae, L. Ziegler, S. Hartley, V. Nikolova-Krstevski, P.R. Rohde, C.A. Ng, F. Sachs, P.A. Gottlieb, B. Martinac, Removal of the Mechanoprotective Influence of the Cytoskeleton Reveals PIEZO1 Is Gated by Bilayer Tension, vol. 7, 2016, pp. 1–13.

[49] C. Bae, F. Sachs, P.A. Gottlieb, The mechanosensitive ion channel Piezo1 is inhibited by the peptide GsMTx4, Biochemistry 50 (2011) 6295–6300, https://doi.org/10.1021/BI200770Q.

[50] W.M. Botello-Smith, W. Jiang, H. Zhang, A.D. Ozkan, Y.C. Lin, C.N. Pham, J.J. Lacroix, Y. Luo, A mechanism for the activation of the mechanosensitive Piezo1 channel by the small molecule Yoda1, Nat. Commun. 10 (2019) 4503, https://doi.org/10.1038/S41467-019-12501-1, 4503.

[51] A. Suarez-Arnedo, F.T. Figueroa, C. Clavijo, P. Arbeláez, J.C. Cruz, C. Muñoz-Camargo, An image J plugin for the high throughput image analysis of in vitro scratch wound healing assays, PLoS One 15 (2020) e0232565, https://doi.org/10.1371/JOURNAL.PONE.0232565.

[52] J. Schindelin, I. Arganda-Carreras, E. Frise, V. Kaynig, M. Longair, T. Pietzsch, S. Preibisch, C. Rueden, S. Saalfeld, B. Schmid, et al., Fiji - an Open Source platform for biological image analysis, Nat. Methods 9 (2012) 676–682, https://doi.org/10.1038/NMETH.2019.

[53] J. Stricker, T. Falzone, M.L. Gardel, Mechanics of the F-actin cytoskeleton, J. Biomech. 43 (2010) 9–14, https://doi.org/10.1016/J.JBIOMECH.2009.09.003.

[54] Z. Zhang, S. Xia, P. Kanchanawong, An integrated enhancement and reconstruction strategy for the quantitative extraction of actin stress fibers from fluorescence micrographs, BMC Bioinf. 18 (2017) 1–14, https://doi.org/10.1186/S12859-017-1684-Y/FIGURES/6.

[55] P. Mishra, D.C. Martin, I.P. Androulakis, P.V. Moghe, Fluorescence imaging of actin turnover parses early stem cell lineage divergence and senescence, Sci. Rep. 9 (2019) 1–12, https://doi.org/10.1038/s41598-019-46682-y, 91 2019.

[56] I. Lüchtefeld, A. Bartolozzi, J. Mejía Morales, O. Dobre, M. Basso, T. Zambelli, M. Vassalli, Elasticity spectra as a tool to investigate actin cortex mechanics, J. Nanobiotechnol. 18 (2020) 1–11, https://doi.org/10.1186/S12951-020-00706-2/FIGURES/5.

[57] M. Schaks, G. Giannone, K. Rottner, Actin dynamics in cell migration, Essays Biochem. 63 (2019) 483–495, https://doi.org/10.1042/EBC20190015.

[58] K. Tanaka, S. Takeda, K. Mitsuoka, T. Oda, C. Kimura-Sakiyama, Y. Maéda, A. Narita, Structural basis for cofilin binding and actin filament disassembly, Nat. Commun. 9 (2018) 1–12, https://doi.org/10.1038/s41467-018-04290-w, 91 2018.
[59] J. Kraus, R.W. Russell, E. Kudryashova, C. Xu, N. Katyal, J.R. Perilla, D.S. Kudryashov, T. Polenova, Magic angle spinning NMR structure of human cofilin-2 assembled on actin filaments reveals isoform-specific conformation and binding mode, Nat. Commun. 13 (2022) 1–12, https://doi.org/10.1038/s41467-022-29595-9, 131 2022.
[60] J. Xu, Y. Huang, J. Zhao, L. Wu, Q. Qi, Y. Liu, G. Li, J. Li, H. Liu, H. Cofilin Wu, A promising protein implicated in cancer metastasis and apoptosis, Front. Cell Dev. Biol. 9 (2021) 55, https://doi.org/10.3389/FCELL.2021.599065/BIBTEX.
[61] S. Shishkin, L. Eremina, N. Pashintseva, L. Kovalev, M. Kovaleva, Cofilin-1 and other ADF/cofilin superfamily members in human malignant cells, Int. J. Mol. Sci. 18 (2017), https://doi.org/10.3390/IJMS18010010.
[62] V. Janssens, J. Goris, Protein phosphatase 2A: a highly regulated family of serine/threonine phosphatases implicated in cell growth and signalling, Biochem. J. 353 (2001) 417–439, https://doi.org/10.1042/0264-6021:3530417.
[63] Y. Chen, X. Wang, miRDB: an online database for prediction of functional microRNA targets, Nucleic Acids Res. 48 (2020) D127–D131, https://doi.org/10.1093/NAR/GKZ757.
[64] K.C. Miranda, T. Huynh, Y. Tay, Y.S. Ang, W.L. Tam, A.M. Thomson, B. Lim, I. Rigoutsos, A pattern-based method for the identification of MicroRNA binding sites and their corresponding heteroduplexes, Cell 126 (2006) 1203–1217, https://doi.org/10.1016/j.cell.2006.07.031.
[65] J. Ding, X. Li, H. Hu, TarPmiR: a new approach for microRNA target site prediction, Bioinformatics 32 (2016) 2768–2775, https://doi.org/10.1093/BIOINFORMATICS/BTW318.
[66] J. Zhang, Y. Zhou, T. Huang, F. Wu, L. Liu, J.S.H. Kwan, A.S.L. Cheng, J. Yu, K.F. To, W. Kang, PIEZO1 functions as a potential oncogene by promoting cell proliferation and migration in gastric carcinogenesis, Mol. Carcinog. 57 (2018) 1144–1155, https://doi.org/10.1002/MC.22831.
[67] Y. Han, C. Liu, D. Zhang, H. Men, L. Huo, Q. Geng, S. Wang, Y. Gao, W. Zhang, Y. Zhang, et al., Mechanosensitive ion channel Piezo1 promotes prostate cancer development through the activation of the Akt/mTOR pathway and acceleration of cell cycle, Int. J. Oncol. 55 (2019) 629–644, https://doi.org/10.3892/IJO.2019.4839.
[68] T. Zhu, J. Guo, Y. Wu, T. Lei, J. Zhu, H. Chen, S. Kala, K.F. Wong, C.P. Cheung, X. Huang, et al., The mechanosensitive ion channel Piezo1 modulates the migration and immune response of microglia, iScience 26 (2023), https://doi.org/10.1016/J.ISCI.2023.105993.
[69] Y. Wang, F. Shibasaki, K. Mizuno, Calcium signal-induced cofilin dephosphorylation is mediated by Slingshot via calcineurin, J. Biol. Chem. 280 (2005) 12683–12689, https://doi.org/10.1074/JBC.M411494200.
[70] M.M.L. Davidson, R.J. Haslam, Dephosphorylation of cofilin in stimulated platelets: roles for a GTP-binding protein and Ca2+, Biochem. J. 301 (Pt 1) (1994) 41–47, https://doi.org/10.1042/BJ3010041.
[71] Actin depolymerizing factor and cofilin phosphorylation dynamics: response to signals that regulate neurite extension - PubMed, Available online: https://pubmed.ncbi.nlm.nih.gov/9484959/. (Accessed 12 February 2024).
[72] N.V. Oleinik, N.I. Krupenko, S.A. Krupenko, ALDH1L1 inhibits cell motility via dephosphorylation of cofilin by PP1 and PP2A, Oncogene 29 (2010) 6233–6244, https://doi.org/10.1038/ONC.2010.356.
[73] C. Kienzle, N. Basnet, A.H. Crevenna, G. Beck, B. Habermann, N. Mizuno, J. von Blume, Cofilin recruits F-actin to SPCA1 and promotes Ca2+-mediated secretory cargo sorting, J. Cell Biol. 206 (2014) 635, https://doi.org/10.1083/JCB.201311052.
[74] F. Morena, C. Argentati, S. Acquati, S. DeWall, F. Kelly, V. Calbi, F. Fumagalli, S. Zancan, A. Biffi, A. Aiuti, et al., Toward reference intervals of ARSA activity in the cerebrospinal fluid: implication for the clinical practice of metachromatic leukodystrophy, J. Appl. Lab. Med. 6 (2021) 354–366, https://doi.org/10.1093/JALM/JFAA108.
[75] F. Morena, I. Armentano, P. Montanucci, C. Argentati, E. Fortunati, S. Montesano, I. Bicchi, T. Pescara, I. Pennoni, S. Mattioli, et al., Design of a nanocomposite substrate inducing adult stem cell assembly and progression toward an Epiblast-like or Primitive Endoderm-like phenotype via mechanotransduction, Biomaterials 144 (2017) 211–229, https://doi.org/10.1016/J.BIOMATERIALS.2017.08.015.
[76] C. Argentati, F. Dominici, F. Morena, M. Rallini, I. Tortorella, A. Ferrandez-Montero, R.M. Pellegrino, B. Ferrari, C. Emiliani, M. Lieblich, et al., Thermal treatment of magnesium particles in polylactic acid polymer films elicits the expression of osteogenic differentiation markers and lipidome profile remodeling in human adipose stem cells, Int. J. Biol. Macromol. 223 (2022) 684–701, https://doi.org/10.1016/J.IJBIOMAC.2022.11.005.
[77] F. Morena, C. Argentati, M. Soccio, I. Bicchi, F. Luzi, L. Torre, A. Munari, C. Emiliani, M. Gigli, N. Lotti, et al., Unpatterned bioactive poly(butylene 1,4-cyclohexanedicarboxylate)-based film fast induced neuronal-like differentiation of human bone marrow-mesenchymal stem cells, Int. J. Mol. Sci. 21 (2020) 9274, https://doi.org/10.3390/IJMS21239274, 9274 2020, 21.